IUST
Iran University of Science and Technology

Iranian Journal of Electrical and Electronic Engineering

Journal Homepage: ijeee.iust.ac.ir

Design of a Fractional Slot Concentrated Winding Double-Speed AFPM Motor

R. Mirzahosseini*(C.A.) and E. Rahimi Namaghi**

Abstract: In this paper, a new topology of fractional slot concentrated winding double rotor axial flux permanent magnet synchronous motor (FSCW-DRAFPMSM) is introduced. The desired structure consists of a nonslotted stator core and two rotor discs. The pole number of the two rotors is different and these two rotors rotate at different speeds in opposite directions. A sample motor with an output power of 200 Watts is designed with the proposed structure. The two rotors of this sample motor rotate with speeds of 1200 and 857 rpm. The Finite Element Method (FEM) is employed to evaluate the performance of the proposed structure. Some performance characteristics of the case study machine, such as the Back EMF, input power, and electromagnetic torques of two rotors are presented to confirm the correctness of the operation of the proposed structure. In addition, the shifting technique is used to improve the Back EMF waveform of the machine. An analytical formula is proposed for calculating the fundamental component of the Back EMF waveform. The accuracy of the formula is approved by FEM.

Keywords: Axial Flux Permanent Magnet (AFPM), Back EMF waveform, Counter-rotating rotors, Fractional slot concentrated winding.

1 Introduction

ELECTRICAL motors are widely used in industrial applications such as electric vehicles, fans, elevators, etc. [1]–[3]. Distributed winding and concentrated winding are two common types of windings that have been used in permanent magnet (PM) machines. High-power density, high efficiency, short-end turn, slow cogging torque, and high slot fill factor are advantages of concentrated winding compared to distributed winding [4]–[7]. Despite these advantages, Concentrated windings produce a nonsinusoidal magnetomotive force (MMF) distribution along the air gap. Hence, the air-gap flux density has many low and high-order spatial harmonics. In PM machines, these harmonics induce significant rotor magnet losses. In asynchronous machines, they cause high rotor bar losses and various parasitic torque components that degrade the machine's average torque. In synchronous reluctance machines, they lead to high torque ripples. Moreover, spatial harmonics cause local saturation, additional stator and rotor losses, acoustic noise, and vibration. Several papers have been studied on concentrated windings [8]. In [9], the design and analysis of fractional slot concentrated winding (FSCW) PM machines have been studied. Also, commercial applications of this structure have been presented. In [10], an overview of recent research in the field of FSCW machine optimization has been presented. The general formulation of the winding factor for the FSCW has been performed. Also, the winding factor is redefined for stator windings without any information on the number of poles [11]. In [12], a generator with FSCW for use in low-voltage applications in distributed generation has been proposed. The generator is designed based on (FE) analysis. In [13], a permanent magnet (PM) vernier motor with FSCW has been introduced. The induced voltage is analyzed through FE simulations and compared with their analytical calculation results. A five-phase FSCW has been presented. One of the advantages of this structure, besides having the advantages of the

Iranian Journal of Electrical & Electronic Engineering, 2023.
Paper first received 28 May 2023 and accepted 27 Dec. 2023.
* The author is with the Department of Electrical and Robotic Engineering, Shahrood University of Technology, Shahrood, Iran.
E-mail: reza.mirzahosseini78@gmail.com
** The author is with the Department of Electrical and Computer Engineering, Semnan University, Semnan, Iran.
E-mail: elhamrahimi1367@yahoo.com
Corresponding Author: R. Mirzahosseini.

conventional FSCW, is weak space harmonics of magnetomotive force (MMF). In the desired structure, a stator shift technique combined with a star/pentagon winding connection has been used. Compared to the conventional model, the first harmonic of MMF in the new winding is eliminated. Moreover, the nonoverlapping characteristics of FSCW are kept. The winding factor of new winding is improved, and the total harmonic distortion (THD) of MMF is reduced by 2.1% [14]. In [15] the effect of the number of winding layers on the performance of FSCW interior permanent magnet machines has been evaluated. Investigation of the results shows that the high number of layers can have a significant improvement in efficiency and torque density. In [16], by both methods of the nonlinear magnetic circuit and FEM, the mechanism of reducing magnetic saturation by the FSCW technique is investigated. A synchronous reluctance machine with FSCW has been introduced. To eliminate the unwanted MMF harmonics, stator shifting has been used. Also, the comprehensive comparisons for the case study machine equipped with FSCW and distributed winding are presented [17].

Our studies show that the researchers in the previous papers tried to mitigate the harmonics of MMF. However, these harmonics can be useful for designing a machine with a new structure. In the present paper, a topology for a nonslotted double rotor AFPM machine is introduced that operates based on harmonics components of MMF. This proposed structure has two rotor discs that rotate in opposite directions.

2 Topology of the Proposed Machine

It is evident that the MMF produced by the stator currents of the machine is not entirely sinusoidal and has harmonics. Generally, decreasing the harmonic components of the stator MMF and increasing the first harmonic order are the main objectives of proposing a new winding arrangement. The fifth and seventh harmonics of the MMF are often the dominant harmonics component of the MMF. These two MMF harmonics rotate in opposite directions. However, if the machine is designed so that the fifth and seventh harmonics have significant amplitudes, we can use these two harmonics to have a machine with two different rotating directions. On the other hand, the pole number of an electrical machine must be an even number. Therefore, it is possible to design a machine with two rotors and one stator disc in a way that one of the rotors has (2×5=10) poles while the other one has (2×7=14) poles. One rotor disc rotates clockwise while the other rotor rotates counterclockwise, independently. Considering that the nominal frequency of the designed machine is equal to 100 Hz, the speeds of the 10-pole and 14-pole rotors are 1200 and 857 rpm, respectively. The FSCW has significant harmonic components compared to distributed winding. Therefore, the FSCW is an excellent choice to have a machine with high amplitudes of fifth and seventh harmonics. The pole arc to pole pitch α_i has a significant influence on the amplitudes of the fifth and seventh harmonics of MMF. By varying the value of α_i can achieve a sinusoidal or trapezoidal Back EMF. This parameter can increase the amplitudes of the fifth and seventh harmonics of the Back EMF. The double-rotor Axial flux permanent magnet (AFPM) machine is a good candidate to have a machine with two opposite directions of rotation simultaneously. The machine topology is shown in Fig 1. The machine structure includes a toroidal wounded stator in the middle and two independent rotors on both sides. The case study machine is an axial flux structure. Therefore, most of the magnetic fluxes pass through the air gap along the axis of the machine. These fluxes pass through the stator core circumferentially. Hence, the stator core is fabricated as a spiral. The high silicon–iron alloy sheet is used to fabricate the spirally laminated stator core. The phenolic resin plate has been used as the nonmagnetic material to ensure that the leakage fluxes of one rotor do not enter the other. In addition, the low-carbon steel is employed for rotor cores. Each rotor disc carries a certain number of PMs placed on the inner surface of the rotor core. The single-layer FSCW has been used in the structure of the proposed topology. The 2-D schematic of the winding arrangement is shown in Fig. 2. In this figure, the direction of the current in each coil is indicated by a dot (.) and a cross (×).

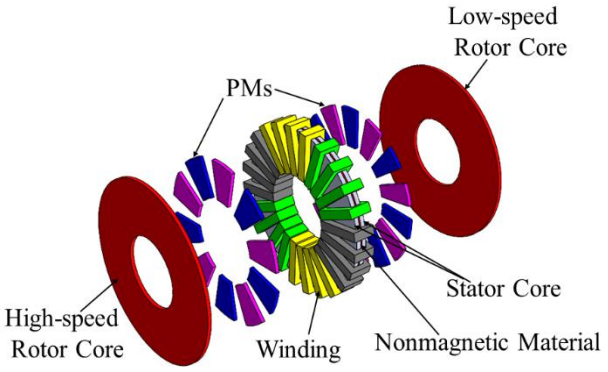

Fig. 1 The structure of the machine.

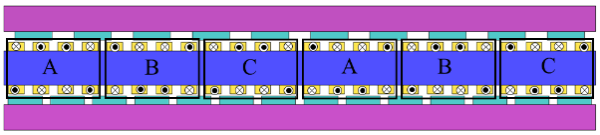

Fig. 2 The winding arrangement of the machine.

3 Evaluating the Operation of the Machine

A sample machine with the specifications given in Table 1 has been designed. The material of the machine's parts is presented in Table 2. To evaluate the performance of the machine, several simulations have been implemented using FEM. As is clear, the structure of the machine is symmetrical. Therefore, to reduce the volume of calculations and save program running time, the 2-D structure of the machine in average diameter is simulated in FE software. The major flux density in the machine is due to the magnetic fluxes of PMs. The magnetic fluxes and induced voltage in the armature windings due to each rotor PMs are obtained easily. For this purpose, by applying the air to the PMs of each rotor, the magnetic fluxes and induced voltage due to the other rotor PMs are attained. In Fig. 3, the magnetic flux distribution due to the high-speed rotor PMs at no-load conditions is shown. In Fig. 4, the magnetic flux distribution due to the low-speed rotor PMs is depicted. The induced voltage in the stator windings due to the high-speed rotor PMs is illustrated in Fig. 5. In addition, Fig. 6 shows the obtained voltage for the low-speed rotor. Comparing the results of two rotors shows that the amplitudes of induced voltages are identical. The total Back EMF is obtained by summing the induced voltages shown in Fig. 4 and Fig. 6. The total Back EMF depends on the initial positions of two rotors. For a better understanding, the values of the fundamental component of Back EMF and its THD for various positions of two rotors are presented in Table 3. According to this table, when two rotors are shifted 13 degrees related to each other, the maximum value of Back EMF is achieved. The Back EMF of the machine with 13 13-degree shifting angle is shown in Fig. 7. As is obvious, the Back EMF waveform is almost sinusoidal. It should be noted that the machine power angle and rotor positions depend on the output power of each rotor disc. The output power of the machine depends on the values of the armature current and Back EMF. Since the current flows in the coil arms on both sides of the stator are identical, the distributed power between two rotor discs directly depends on the values of induced voltages due to each rotor PMs. It should be noted that the location of each rotor disc affects the amplitude of the Back EMF waveform. Therefore, for simplicity, the machine has been designed so that two rotor discs have identical output power and consequently similar Back EMF amplitude and positions. The case study machine is a permanent magnet synchronous machine type. Therefore, this structure has no starting torque. In this case, this machine must be run with a drive system. It should be noted that the initial positions of the rotors have a significant effect on the transient and steady-state performance characteristics of the machine. Therefore, the positions and speeds of the two rotors are controlled with an absolute encoder and drive system. The purpose of this paper is to evaluate the performance characteristics of the machine in the steady-state condition. For this goal, the machine has been tested under full load conditions. For this purpose, a load with a power of 100 watts has been applied to each rotor disc. The three-phase stator current of the machine is shown in Fig. 8. These currents produced two counter-rotating fields in the air gap. For better investigation, the air gap flux density due to the stator currents has been obtained. Fig. 9 shows the air-gap flux density and the amplitude of corresponding harmonics. As is clear, the fifth and seventh harmonics are the dominant components in the air-gap flux density waveform. According to this figure, the amplitude of the first harmonic is not significant compared to the fifth and seventh harmonics. Therefore, this harmonic has no significant influence on the performance characteristics of the machine.

Table 1 Machine specifications.

Parameter	Value
The output power of each rotor (P_{out})	100 (Watt)
Speed of 10-pole rotor (n_{mh})	1200 (rpm)
Speed of 14-pole rotor (n_{ml})	857 (rpm)
The axial length of the stator core (l_{cs})	15 (mm)
The axial length of PMs (l_{pm})	5 (mm)
The axial length of the rotor core (l_{cr})	7 (mm)
The thickness of the winding (l_w)	5 (mm)
The outer diameter of the machine (D_o)	220 (mm)
The inner diameter of the machine (D_i)	113.6 (mm)
The air gap length (g)	1 (mm)
The number of turns of each coil	160
Current density (J)	6 (A/mm^2)
Fill factor	0.5

Table 2 Materials of the cores, PM, and windings.

Parameter	Material
Stator	High silicon–iron alloy
Rotor	Low-carbon steel
PM	NdFeB (N42)
Winding	Copper
Nonmagnetic material	Phenolic resin

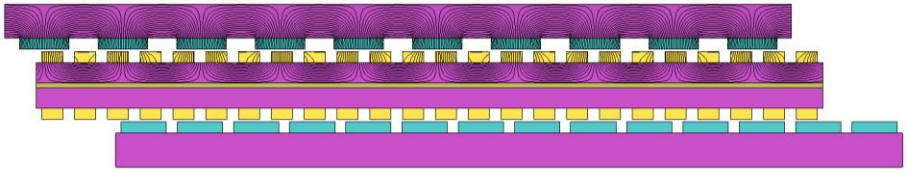

Fig. 3 Magnetic Flux path in the machine due to the high-speed rotor PMs.

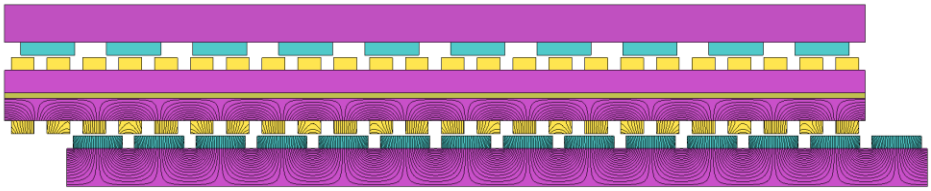

Fig. 4 Magnetic Flux path in the machine due to the low-speed rotor PMs.

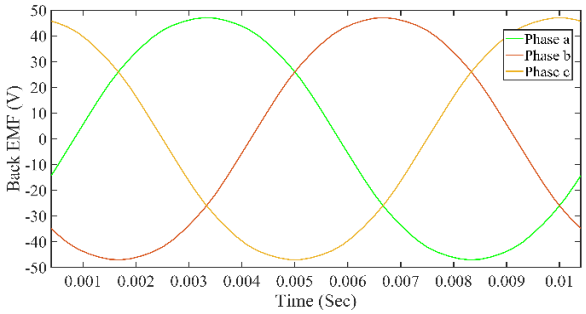

Fig. 5 The induced voltage in the armature windings due to the high-speed rotor PMs.

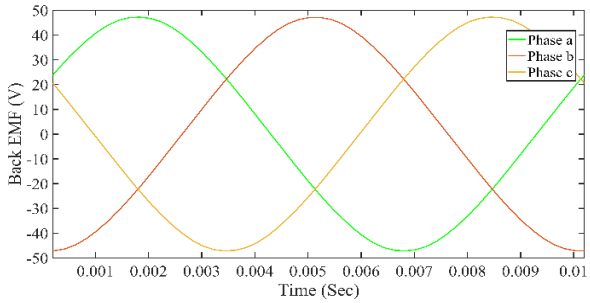

Fig. 6 The induced voltage in the armature windings due to the low-speed rotor PMs.

Table 3 The value of Back EMF for different relative positions of two rotors.

The relative position (Degree)	The amplitude of the fundamental component (V)	THD (%)
2.6	31.5	24.2
5.2	57.3	5.7
7.8	76.7	3.3
10.4	90	2.43
12	93.4	1.2
13	**94**	**0.8**
14.6	92.4	1.85
15.6	89	2.7

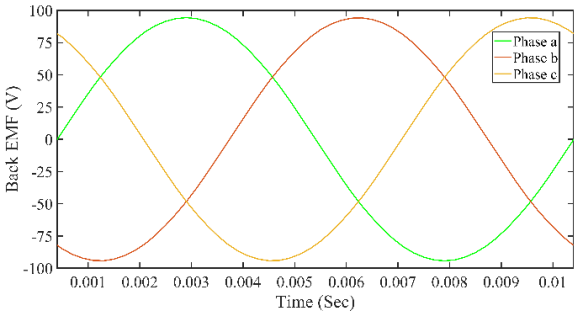

Fig. 7 The Back EMF of the machine.

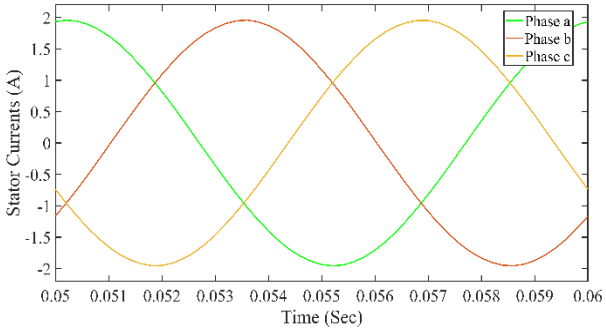

Fig. 8 Three-phase of stator current.

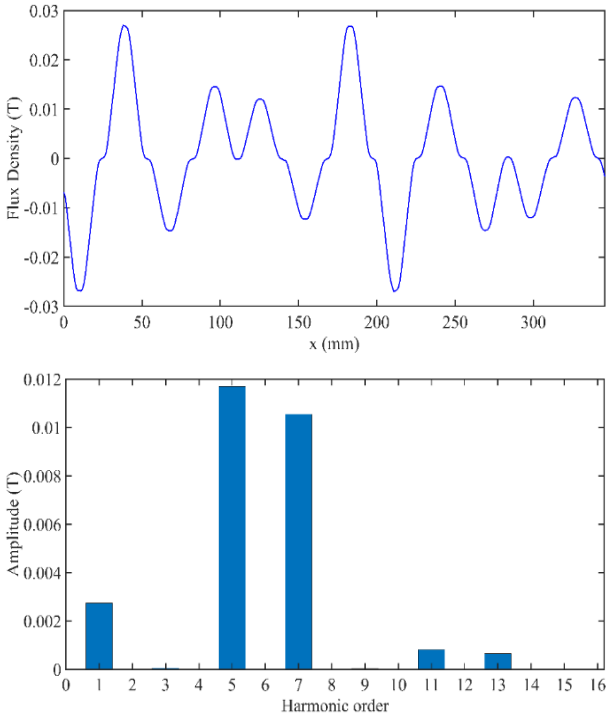

Fig. 9 The air gap flux density due to stator currents and its harmonic components.

The input power of the case study machine is shown in Fig. 10. For calculating the instantaneous value of the input power, the instantaneous values of the currents and terminal voltages are multiplied. Then, the average value of the input power is obtained. One of the disadvantages of this structure is the unbalanced magnetic forces. In the case study structure, the fields produced by the stator currents apply forces to each rotor. Reciprocally, each of the rotors also applies forces to the stator. The components of these forces can be obtained in three

directions x, y, z. The components of these forces along the x-axis cause the rotors to move. However, two other components cause the machine structure to vibrate. The electromagnetic force produced by Stator currents and applied to the low-speed rotor and the high-speed rotor along the x and y-axis are indicated in Fig. 11 and Fig. 12. In addition, simulation results show that the forces along the z-axis are very small and can be ignored. As is clear, the differences between the forces applied to the two rotors are not significant. However, these minor differences cause vibration and acoustic noises.

Based on the linear speed and the average radius of the machine, the angular speed of the machine is calculated as:

$$\omega = v / r \tag{1}$$

In which ω, v, and r are the rotor angular speed, linear speed, and average radius, respectively. Also, the output power is obtained as:

$$P_{out} = T\omega = r.F.\omega \tag{2}$$

where P_{out}, T, and F are the output power, electromagnetic torque, and electromagnetic force, respectively. By substituting Eq. (1) in Eq. (2), we have:

$$P_{out} = F.v \tag{3}$$

The linear speed of two rotor discs is shown in Fig. 13. With the help of Eq. (3), the output power of two rotor discs is calculated. Calculations confirm that the output power of each rotor disc is 100 watts.

By obtaining the output power, the efficiency is calculated as:

$$\eta = \frac{P_{out}}{P_{in}} \tag{4}$$

where P_{in} is the input power. With the help of Eq. (4), the efficiency of the machine would be equal to 76%.

The obtained results confirm that the machine has acceptable performance characteristics.

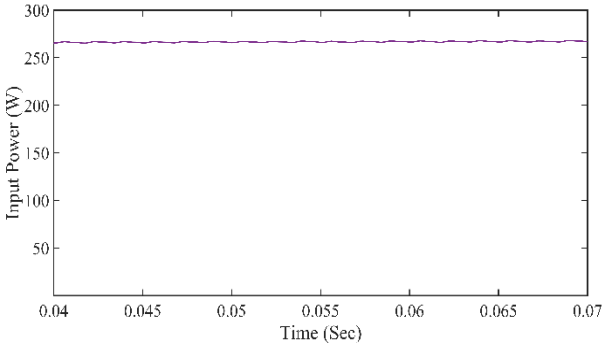

Fig. 10 Input power of the machine.

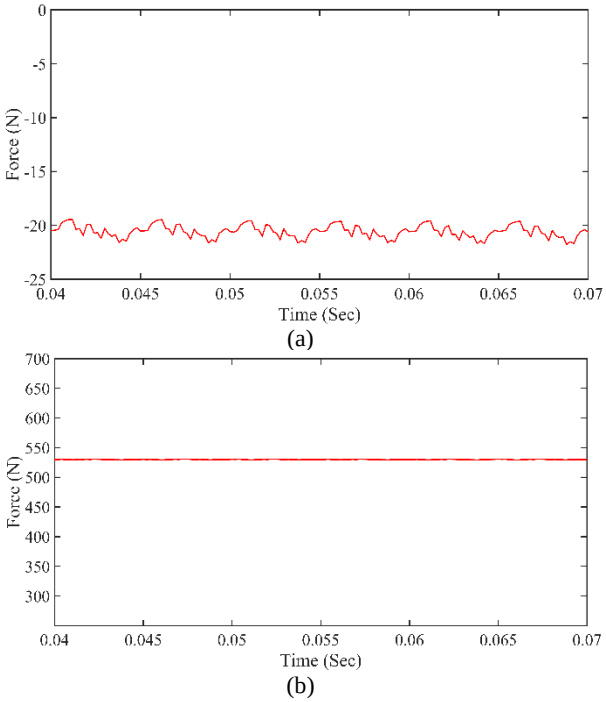

Fig. 11 The electromagnetic force applied to the low-speed rotor a) along the x-axis b) along the y-axis.

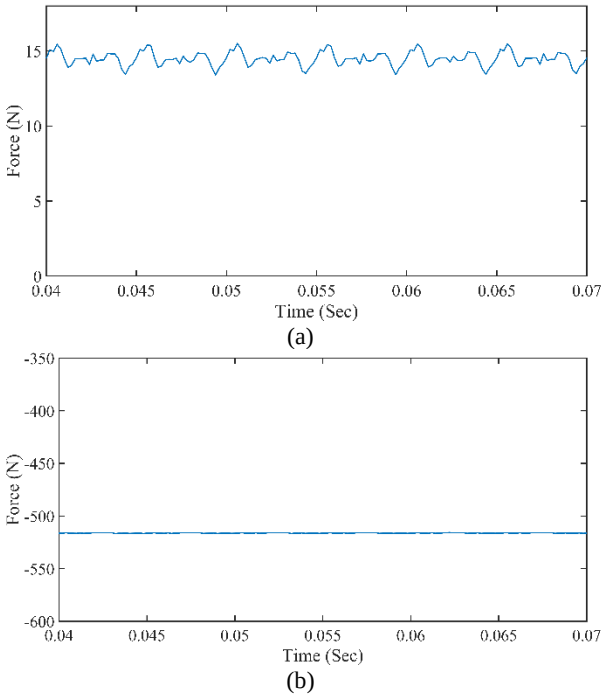

Fig. 12 The electromagnetic force applied to the high-speed rotor a) along the x-axis b) along the y-axis.

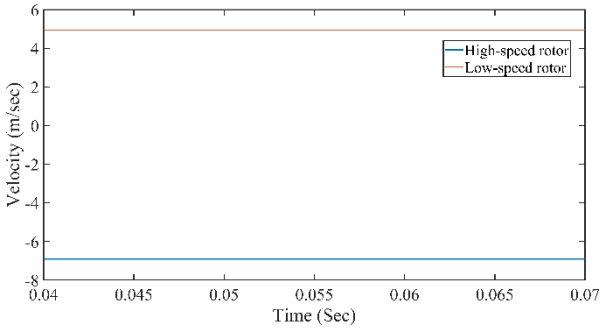

Fig. 13 The linear speed of two rotors.

4 Analytical Calculation of the Back EMF Waveform

The machine structure has a nonslotted stator core. Hence, there are no spatial harmonic components in the Back EMF waveform due to the stator slots. As is obvious From Fig. 7, the Back EMF waveform of the machine is close to a sinusoidal waveform. Furthermore, the fundamental component of the Back EMF produces output power. Therefore, this component has a significant effect on the performance characteristics of the case study structure. For these reasons, in the present paper, a formula is extracted for calculating the fundamental component of the Back EMF. To fulfill this goal, the calculations are done at the machine's average diameter. A section of the two-dimensional (2-D) model of the machine at the average diameter is shown in Fig. 14.

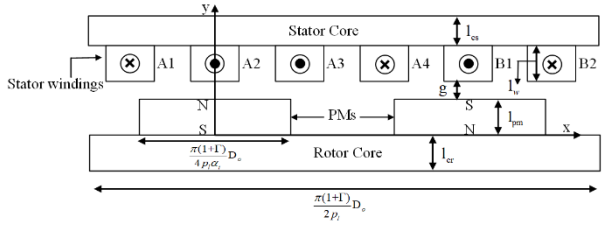

Fig. 14 A section of the 2-D structure of the machine.

Regarding the drops of MMF in the stator and rotor cores in position x_0 by $MMF_{cs}(x_0)$ and $MMF_{cr}(x_0)$, the PM remanent flux density B'_r is obtained as [18]:

$$B_r^{'}(x_0) = B_r[1-(MMF_{cs}(x_0)+MMF_{cr}(x_0))/(2H_{cb}l_{pm})] \quad (5)$$

Where x_0, B_r, H_{cb}, and l_{pm} are a number in the range of [0, τp/2], PM remanent flux density, PM coercive force, and thickness of PM, respectively. The values of B'_r for various values of x_0 are calculated using (5). After that, a Fourier series is applied to the values of $B'_r(x_0)$ as follows [18]:

$$B_r^{'}(x_0) = b_0 + b_1\cos(\xi x_0+\gamma_1) + b_2\cos(2\xi x_0+\gamma_2) \quad (6)$$

Where parameters b_0, b_1, ξ, γ_1, b_2, and γ_2 are defined with the help of the technique of curve fitting.

The magnetization vector function $M'_y(x)$ for various values of y between 0 and l_{pm} is attained as [18]:

$$M_y^{'}(x) = \sum_{n=1,3,5,\ldots}^{\infty}((K_n^{'}/\mu_0)\cos(n\pi x/\tau_p)) = \begin{cases} \pm B_r/\mu_0 & in\ PM\ materials \\ 0 & in\ airgap\ area\ between\ PMs \end{cases} \quad (7)$$

Where τ_p, and μ_0 are the length of pole pitch at the average diameter, and permeability of the air, respectively. The coefficient K'_n for the fundamental component is calculated as [18]:

$$\begin{aligned} K_1^{'} &= (4b_0/(\pi))sin(a\pi/2) \\ &-(4b_1\xi\tau_p/(\xi^2\tau_p^2-\pi^2))\sin\gamma_1 \\ &-(8b_2\xi\tau_p/(4\xi^2\tau_p^2-\pi^2))\sin\gamma_2 \\ &+(2b_1/(\xi\tau_p+\pi))\sin((a(\xi\tau_p+\pi)/2)+\gamma_1) \\ &+(2b_1/(\xi\tau_p-\pi))\sin((a(\xi\tau_p-\pi)/2)+\gamma_1) \\ &+(2b_2/(2\xi\tau_p+\pi))sin((a(2\xi\tau_p+\pi)/2)+\gamma_2) \\ &+(2b_2/(2\xi\tau_p-\pi))\sin((a(2\xi\tau_p-\pi)/2)+\gamma_2) \end{aligned} \quad (8)$$

The vertical components of the magnetic flux density in the winding zone for $l_{pm}+g<y<l_{pm}+g+l_w$ are determined as:

$$\begin{aligned} B_{yI}(x,y,t) &= (K_1^{'}/2)(1-e^{S_1})/(1-e^{S_2})(e^{S_3}+e^{S_4}) \\ &\times cos(((4p_l x/((1+\Gamma)D_o))-p_l\theta_m(t))) \\ S_1 &= \left(-8p_l l_{pm}\right)/\left((1+\Gamma)D_0\right) \\ S_2 &= \left(-8p_l(g+l_w+l_{pm})\right)/\left((1+\Gamma)D_0\right) \\ S_3 &= 4p_l\left(l_{pm}-y\right)/\left((1+\Gamma)D_0\right) \\ S_4 &= (-4p_l\left(2g+2l_w+l_{pm}-y\right))/\left((1+\Gamma)D_0\right) \end{aligned} \quad (9)$$

In which g, l_w, p_l, Γ, D_o are the length of the air gap, axial length of winding, pole pair number of the low-speed rotor, inner to outer diameter ratio of the stator core, and outer diameter of the stator core, respectively. In addition, $\theta_m(t)$ represents the angular location of the middle of pole N relating to the middle of coil A1.

After determining $B_{yI}(x,y,t)$, the flux linkage of one coil is attained as:

$$\begin{aligned} &\varphi_{PH\_PM}(t) = (p_l(1-\Gamma)D_o/2a_p) \\ &\times\sum_{i=1}^{N_{layer}}\sum_{j=1}^{N_{Turnlayer}\{i\}}\int_{((\tau_p\theta_{PH}/\pi)+\Delta x_{ij})}^{((\tau_p\theta_{PH}/\pi)+\Delta x_{ij}+\tau_p)} B_{yI}(x.l_{pm}+g+0.5l_w-\Delta y_{ij}.t)dt \\ &=((1+\Gamma)D_o/(4a_p)) \\ &\times\sum_{i=1}^{N_{layer}}\sum_{j=1}^{N_{Turnlayer}\{i\}}(K_1^{'}(1-\Gamma)D_o/2)(e^{S_5}+e^{S_6})/(1-e^{S_2})(1-e^{S_1}) \\ &\times sin((p_l\theta_m(t)-\theta_{PH}-((4p_l\Delta x_{ij})/((1+\Gamma)D_o)))) \\ &S_5 = (4p_l\left(-g-0.5l_w+\Delta y_{ij}\right))/\left((1+\Gamma)D_0\right) \\ &S_6 = (-4p_l\left(g+1.5l_w+\Delta y_{ij}\right))/\left((1+\Gamma)D_0\right) \end{aligned} \quad (10)$$

where a_p, N_{layer}, $N_{Turnlayer}\{i\}$, Δx_{ij} and Δy_{ij} represent the number of parallel paths of the stator winding, the number of stator winding layers, the number of windings

turns in the i-th layer, the horizontal and vertical distances of the conductor placed in column j of layer i from the middle of winding, correspondingly. In addition, the θ_{PH} represents the phase angle. The value of this parameter for phase A is zero.

By derivating from flux linkage, the induced voltage in arms A1 of winding of phase A is calculated as:

$$E_{PH1}(t)=(((1-\Gamma^2)D_o^2 p_l \omega_{ml}(t))/(8a_p))$$
$$\times\sum_{i=1}^{N_{layer}}\sum_{j=1}^{N_{Turnlayer}\{i\}}\begin{pmatrix}K_1^{'}(e^{S_5}+e^{S_6})/(1-e^{S_2})(1-e^{S_1})\\ \times\cos[(p_l\theta_m(t)-\theta_{PH}-((4p_l\Delta x_{ij})/((1+\Gamma)D_o)))]\end{pmatrix} \quad (11)$$

where $\omega_{ml}(t)$ is the angular speed of the low-speed rotor. A similar procedure is used to calculate the induced voltages in other arms of winding of phase A. However, the voltage of each arm has a shift angle related to the other arms. Hence, the induced voltages in the adjacent arms of winding of phase A are determined as:

$$E_{PH1\_K}(t)=(((1-\Gamma^2)D_o^2 p_l \omega_{ml}(t))/(8a_p))$$
$$\times\sum_{i=1}^{N_{layer}}\sum_{j=1}^{N_{Turnlayer}\{i\}}\begin{pmatrix}K_1^{'}(e^{S_5}+e^{S_6})/(1-e^{S_2})(1-e^{S_1})\\ \times\cos[(p_l\theta_m(t)-(2\pi p_l(K-1)/N_l)\\ -\theta_{PH}-((4p_l\Delta x_{ij})/((1+\Gamma)D_o)))]\end{pmatrix} \quad (12)$$

where, K is an integer number in the range of [1, 4]. As is obvious from Fig. 14, the winding of phase A on the low-speed side has 8 arms in which 4 arms are shifted 180 degrees with respect to the other 4 arms. Hence, the induced voltage in these four arms of winding of phase A is defined as follows:

$$E_{PH2\_K}(t)=(((1-\Gamma^2)D_o^2 p_l \omega_{ml}(t))/(8a_p))$$
$$\times\sum_{i=1}^{N_{layer}}\sum_{j=1}^{N_{Turnlayer}\{i\}}\begin{pmatrix}K_1^{'}(e^{S_5}+e^{S_6})/(1-e^{S_2})(1-e^{S_1})\\ \times\cos[(p_l\theta_m(t)-(2\pi p_l(K-1)/N_l)\\ -\pi-\theta_{PH}-((4p_l\Delta x_{ij})/((1+\Gamma)D_o)))]\end{pmatrix} \quad (13)$$

The induced voltage in the arms of stator windings on the low-speed side is obtained as:

$$\begin{aligned}E_{PH\_low}(t)&=E_{PH1\_K}(t)+E_{PH2\_K}(t)\\&=E_{PH1\_1}(t)-E_{PH1\_2}(t)-E_{PH1\_3}(t)+E_{PH1\_4}(t)\\&+E_{PH2\_1}(t)-E_{PH2\_2}(t)-E_{PH2\_3}(t)+E_{PH2\_4}(t)\end{aligned} \quad (14)$$

In this case, the induced voltage will be equal to:

$$E_{PH\_low}(t)=(((1-\Gamma^2)D_o^2 p_l \omega_{ml}(t))/(8a_p))$$
$$\times\sum_{i=1}^{N_{layer}}\sum_{j=1}^{N_{Turnlayer}\{i\}}\begin{pmatrix}K_1^{'}(e^{S_5}+e^{S_6})/(1-e^{S_2})(1-e^{S_1})\\ \times(\cos((p_l\theta_m(t)-\theta_{PH}-((4p_l\Delta x_{ij})/((1+\Gamma)D_o))))\\ -\cos((p_l\theta_m(t)-(2\pi p_l/N_l)-\theta_{PH}-((4p_l\Delta x_{ij})/((1+\Gamma)D_o))))\\ -\cos((p_l\theta_m(t)-(4\pi p_l/N_l)-\theta_{PH}-((4p_l\Delta x_{ij})/((1+\Gamma)D_o))))\\ +\cos((p_l\theta_m(t)-(6\pi p_l/N_l)-\theta_{PH}-((4p_l\Delta x_{ij})/((1+\Gamma)D_o)))))\end{pmatrix} \quad (15)$$

Using an identical method, the induced voltages in the stator windings on the high-speed side are determined. In this case, the induced voltage in the arms of winding of phase A on the high-speed side is calculated as:

$$E_{PH\_high}(t)=(((1-\Gamma^2)D_o^2 p_h \omega_{mh}(t))/(8a_p))$$
$$\times\sum_{i=1}^{N_{layer}}\sum_{j=1}^{N_{Turnlayer}\{i\}}\begin{pmatrix}K_1^{'}(e^{S_9}+e^{S_{10}})/(1-e^{S_8})(1-e^{S_7})\\ \times(\cos((p_h\theta_m(t)-\theta_{PH}-\theta_{initial}-((4p_h\Delta x_{ij})/((1+\Gamma)D_o))))\\ -\cos((p_h\theta_m(t)-(2\pi p_h/N_l)-\theta_{PH}-\theta_{initial}-((4p_h\Delta x_{ij})/((1+\Gamma)D_o))))\\ -\cos((p_h\theta_m(t)-(4\pi p_h/N_l)-\theta_{PH}-\theta_{initial}-((4p_h\Delta x_{ij})/((1+\Gamma)D_o))))\\ +\cos((p_h\theta_m(t)-(6\pi p_h/N_l)-\theta_{PH}-\theta_{initial}-((4p_h\Delta x_{ij})/((1+\Gamma)D_o)))))\end{pmatrix}$$
$$\begin{aligned}S_7&=(-8p_h l_{pm})/((1+\Gamma)D_0)\\S_8&=(-8p_h(g+l_w+l_{pm}))/((1+\Gamma)D_0)\\S_9&=(4p_h(-g-0.5l_w+\Delta y_{ij}))/((1+\Gamma)D_0)\\S_{10}&=(-4p_h(g+1.5l_w+\Delta y_{ij}))/((1+\Gamma)D_0)\end{aligned} \quad (16)$$

where $\omega_{mh}(t)$, p_h, $\theta_{initial}$ are the angular speed of the high-speed rotor, the number of pole pairs of the high-speed rotor, and the initial position of the high-speed rotor related to the low-speed rotor, respectively. When induced voltages in all arms of each phase are determined, the Back EMF waveforms of that phase are defined easily. For this goal, the Back EMF waveform is determined by summing the induced voltages as follows:

$$E_{PHmain}(t)=E_{PH\_low}(t)+E_{PH\_high}(t) \quad (17)$$

The fundamental component of the Back EMF has been calculated using FEM and the proposed analytical formula. The waveforms obtained from these two procedures have been illustrated in Fig. 15. As is clear, the result of the analytical formula has good agreement with the result of FEM. For a precise comparison of the results, the Normalized Root Mean Square Error (NRMSE) technique has been used. The percent NRMSE between the results of the analytical formula and FEM is about 4.8%. This minor difference confirms the precision of the proposed formula. Therefore, the proposed formula can be used for determining the fundamental component of the machine Back EMF waveform.

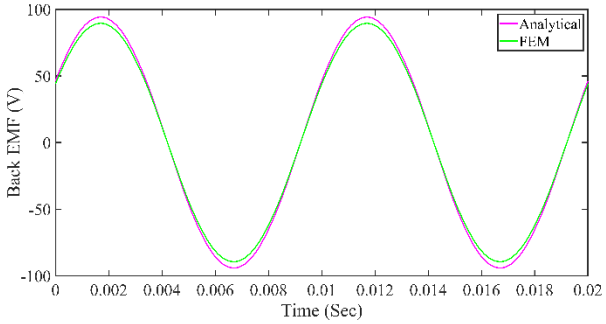

Fig. 15 The fundamental component of the Back EMF attained from FEM and the proposed formula.

5 Conclusion

In this paper, a new structure of the FSCW-DRAFPMSG has been introduced. The case study machine consists of two permanent magnet rotors with different numbers of poles and different rotating directions. This structure has the ability to rotate in opposite directions at different speeds. The FEM has been used to validate the performance characteristics of the proposed topology. The obtained results show that the machine has a maximum amplitude of Back EMF when two rotor discs are shifted 13 degrees related to each other. In addition, each rotor disc produces 100 watts of power while one rotor rotates at a speed of 1200 rpm and the other one rotates at a speed of 857 rpm. Also, the efficiency of the machine is 76%. This structure is suitable for use in several industrial applications, such as gearless elevators or direct-drive ship propulsion systems. An analytical formula has been proposed for calculating the fundamental component of the machine Back EMF. The precision of the formula has been evaluated with the help of FEM. The difference between the results of FEM and the suggested formula is about 4.8%. Therefore, the suggested formula has high precision.

References

[1] M. R. Sreejith, S. Krishnan, and A. Harikrishnan, "Control methods of sine-cosine motor for space application," in *2018 IEEE International Conference on Power Electronics, Drives and Energy Systems (PEDES)*, IEEE, 2018, pp. 1–5.

[2] T. M. Jahns, "The expanding role of PM machines in direct-drive applications," in *2011 International Conference on Electrical Machines and Systems*, IEEE, 2011, pp. 1–6.

[3] J. Piech, "Permanent magnet machines for elevators in super high-rise buildings," *Counc. Tall Build. Urban Habitat CTBUH*, p. 823, 2014.

[4] J. Cros and P. Viarouge, "Synthesis of high performance PM motors with concentrated windings," *IEEE Trans. energy Convers.*, vol. 17, no. 2, pp. 248–253, 2002.

[5] F. Magnussen and C. Sadarangani, "Winding factors and Joule losses of permanent magnet machines with concentrated windings," in *IEEE International Electric Machines and Drives Conference, 2003. IEMDC'03.*, IEEE, 2003, pp. 333–339.

[6] Z. Q. Zhu, Z. Azar, and G. Ombach, "Influence of additional air gaps between stator segments on cogging torque of permanent-magnet machines having modular stators," *IEEE Trans. Magn.*, vol. 48, no. 6, pp. 2049–2055, 2011.

[7] J. Cros, S. Astier, M. Lajoie-Mazenc, and D. Harribey, "A brushless actuator for automotive applications," in *Proc. ICEM'92*, 1992.

[8] M. Valavi, A. Nysveen, R. Nilssen, R. D. Lorenz, and T. Rølvåg, "Influence of pole and slot combinations on magnetic forces and vibration in low-speed PM wind generators," *IEEE Trans. Magn.*, vol. 50, no. 5, pp. 1–11, 2013.

[9] A. M. El-Refaie, "Fractional-slot concentrated-windings synchronous permanent magnet machines: Opportunities and challenges," *IEEE Trans. Ind. Electron.*, vol. 57, no. 1, pp. 107–121, 2009.

[10] G. Dajaku, S. Spas, and D. Gerling, "Advanced optimization methods for fractional slot concentrated windings," *Electr. Eng.*, vol. 101, no. 1, pp. 103–120, 2019.

[11] Y. Yokoi, T. Higuchi, and Y. Miyamoto, "General formulation of winding factor for fractional-slot concentrated winding design," *IET Electr. Power Appl.*, vol. 10, no. 4, pp. 231–239, 2016.

[12] P. Andrada Gascón, B. Blanqué Molina, E. Martínez Piera, M. Torrent Burgués, J. A. Sánchez López, and J. I. Perat Benavides, "Fractional-slot permanent magnet synchronous generator for low voltage applications," *Electr. Eng. Electron. J.*, vol. 1, no. 2, 2013.

[13] B. Kim, "Investigation on slot–pole combinations of a PM vernier motor with fractional-slot concentrated winding configurations," *Energies*, vol. 10, no. 9, p. 1310, 2017.

[14] B. Zhao, J. Gong, T. Tong, Y. Xu, E. Semail, and N.-K. Nguyen, "A novel five-phase fractional slot concentrated winding with low space harmonic contents," *IEEE Trans. Magn.*, vol. 57, no. 6, pp. 1–5, 2021.

[15] P. B. Reddy, A. M. El-Refaie, and K.-K. Huh, "Effect of number of layers on performance of fractional-slot concentrated-windings interior permanent magnet machines," *IEEE Trans. Power Electron.*, vol. 30, no. 4, pp. 2205–2218, 2014.

[16] T. Gundogdu and G. Komurgoz, "Implementation of fractional slot concentrated winding technique to large salient-pole synchronous generators & development with permanent magnets," *Electr. power Syst. Res.*, vol. 105, pp. 57–70, 2013.

[17] S. M. Taghavi Araghi, A. Kiyoumarsi, and B. Mirzaeian Dehkordi, "Synchronous reluctance machines with new type of fractional-slot concentrated-windings based on the concept of stator slot shifting," *IET Electr. Power Appl.*, vol. 17, no. 1, pp. 92–108, 2023.

[18] R. Mirzahosseini, A. Darabi, and M. Assili,

"Analytical and experimental analysis of Back EMF waveform of a TORUS-type non-slotted axial flux permanent magnet synchronous machine with shifted rotor," *Meas. J. Int. Meas. Confed.*, vol. 156, no. 107620, 2020.

Reza Mirzahosseini was born in Gorgan, Iran in 1988. He received his B.Sc., M.Sc., and Ph.D. degrees in electrical engineering from the Shahrood University of Technology, Shahrood, Iran, in 2010, 2013, and 2020, respectively. His research interests include the design and modeling of electrical machines and the implementation of advanced control strategies in machine drives for industrial applications.

Elham Rahimi Namaghi was born in Mashhad, Iran, in August 1988. She received her B.Sc. degree from Birjand University, Birjand, Iran, in 2011. In addition, she received her M.Sc. degree from the Shahrood University of Technology, Shahrood, Iran, in 2016. She received her Ph.D. degree from Semnan University, Semnan, Iran, in 2023. Her research interests include the design, simulation, and control of electrical machines.